ORIGINAL ARTICLE

Seasonal pathways of the Tsugaru Warm Current revealed by high-frequency ocean radars

Tomomi Yasui[1] · Hiroto Abe[1,2] · Toru Hirawake[1,3] · Ken'ichi Sasaki[2] · Masahide Wakita[2]

Abstract

Seasonal pathway of the Tsugaru Warm Current (TWC), coastal boundary current flowing eastward from the Sea of Japan to the North Pacific Ocean, is investigated using data of surface currents measured by high-frequency ocean radars for the period 2014–2020. The TWC takes a pathway along the center of Tsugaru strait during summer season (41.64°N), while during winter season the TWC moves to south to flow along the southern coast (41.55°N). These pathways are associated with seasonal outflow modes known as "Gyre mode" and "Coastal mode," respectively. Seasonal changes in current velocity, characterized by intensified flow in summer and autumn seasons and weakened flow in winter season, are well correlated with seasonal changes of sea level difference between Fukaura and Hakodate. However, this clear relationship is not seen at the eastern exit of the strait (141.5°E). There is a shallow sill that extends northward from the southern coast. HFR further reveals that Coastal mode is locally intensified and widened when passing through this sill. These TWC's responses are qualitatively explained by mass conservation for barotropic flow that flows in a horizontal two-dimensional channel with sea floor depth change. These responses over the sill are not seen during Gyre mode because the northward shift keeps the pathway away from the sill. During the Coastal mode, there are some cases in which the TWC does not ride on the sill but takes a pathway around the sill. Such patterns are seen when the TWC is weak, thus a weak Coastal mode.

Keywords Tsugaru Warm Current · Seasonal variability · Coastal mode · Bathymetry · Sill

1 Introduction

The Tsugaru Warm Current (TWC) is a coastal boundary current that flows into the North Pacific Ocean from the Sea of Japan (Fig. 1a). As one of the branch flows of the Tsushima Warm Current, which originates from the Taiwan Current/Kuroshio (Isobe 1999), the TWC supplies warm, saline water into the North Pacific Ocean. The TWC is driven by the sea level difference (SLD) between the Sea of Japan and the Pacific Ocean (Toba et al. 1982). Ship-board acoustic

Doppler current profiler (ADCP) observation by Ito et al. (2003) revealed that the volume transport of the TWC is 1.5 Sverdrup (Sv, where $1 \text{ Sv} = 1 \times 10^6 \text{ m}^3 \text{ s}^{-1}$) on an annual-mean basis. This is comparable to the 0.91 Sv of the Soya Warm Current (Ohshima et al. 2017) and the 2.60–2.65 Sv of the Tsushima Warm Current (Takikawa et al. 2005; Takikawa and Yoon 2005; Fukudome et al. 2010). The seasonality of TWC volume transport is characterized by an increase in summer and a decrease in winter with ± 0.3 Sv annual amplitude, showing a clear correlation with SLD between the Sea of Japan and the Pacific Ocean (Nishida et al. 2003). Similar seasonal variations and their mechanisms have been reported in the Tsushima Warm Current (Toba et al. 1982) and Soya Warm Current (Ebuchi et al. 2006). Kida et al. (2016) showed seasonal volume transports of the Tsugaru, Tsushima, and Soya Warm Current are in the same phase.

A key difference is that, unlike the Tsushima and Soya Warm Currents, the TWC exhibits two seasonal outflow modes called "Gyre mode" and "Coastal mode" (Conlon 1982). Gyre mode is characterized by the presence of a warm anticyclonic eddy in the warm months including

✉ Tomomi Yasui
  yasuifish@gmail.com

1 Graduate School/Faculty of Fisheries Sciences, Hokkaido University, 3-1-1 Minato-cho, Hakodate, Hokkaido 041-8611, Japan

2 Mutsu Institute for Oceanography, Research Institute for Global Change, Japan Agency for Marine–Earth Science and Technology (JAMSTEC), Aomori, Japan

3 Present address: National Institute of Polar Research, 10-3, Midori-cho, Tachikawa, Tokyo 190-8518, Japan
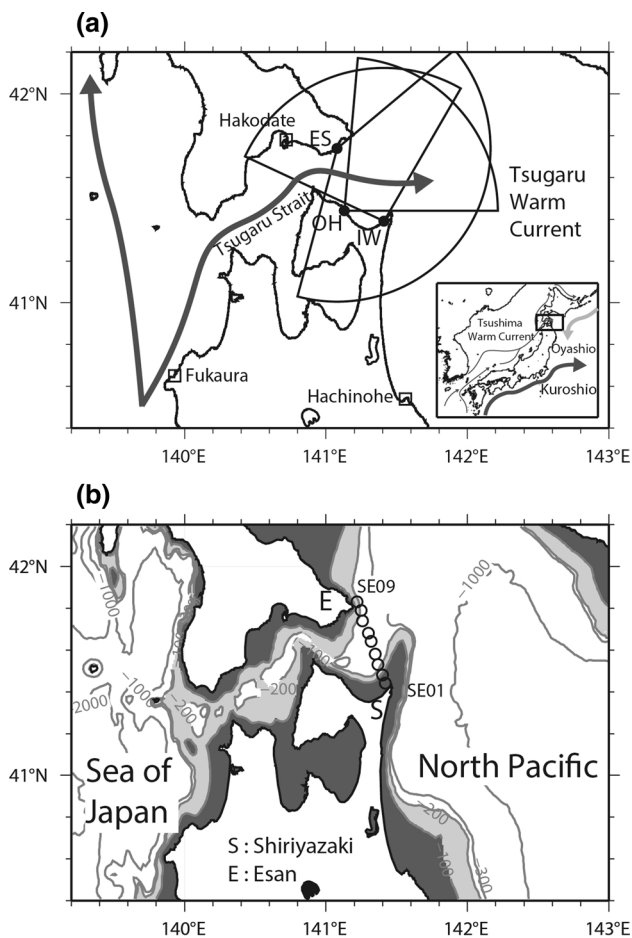
Fig. 1 **a** Geography of the Tsugaru Strait showing spatial coverage of the three high-frequency ocean radar (HFR) stations (black circle symbols): Ohata (OH), Iwaya (IW), and Esan (ES) stations. Two-dimensional surface current data were obtained in areas where two or three HFR coverages overlapped. Locations of tide-gauge stations at Hakodate, Fukaura and Hachinohe are represented as well (open square symbols). **b** Bathymetry chart of the Tsugaru Strait and surrounding regions. Seafloor depths at 100, 200, 300, 1000, and 2000 m are represented by contours, with shallow coastal areas shaded in light gray (<200 m) and dark gray (<100 m). Hydrographic transect along Shiriyazaki–Esan line consists of 9 stations from SE01 (southernmost) to SE09 (northernmost), marked as individual dots along the SE-line

October and November that extends to the east off the strait, while Coastal mode is characterized by flow confined near the coast of the main island of Japan in the cold months including month from December to March (Conlon 1982). The presence of these two outflow modes has been reported by Whitehead and Miller (1979) in laboratory experiments. Many previous studies use terms "Tsugaru Warm Water" (TWW, or TWC water) and "Coastal Oyashio Water" (COW) to distinguish water in this region (e.g., Shimizu et al. 2001; Wakita et al. 2021). The warm-saline TWW is the water transported by the TWC from the west, while the cold-fresh COW flows along the southern coast of Hokkaido

island from the northeast, which has been considered to have its origin in the melted drift ice of Okhotsk Sea (Ohtani et al. 1971). TWW is defined as water with a salinity range of 33.7–34.2, water temperature $>5ºC$, and potential density >24 kg m^{-3}, while COW is defined as water with a salinity range of 32.0–33.0 and a water temperature of 0 °C–2 °C (Hanawa and Mitsudera 1987). The core of the Tsugaru Warm Gyre (Kubokawa 1991) formed in the warm season remains in the subsurface layer in the cold season, covered by lighter Coastal Oyashio Water at the surface (Shimizu et al. 2001; Kobayashi et al. 2014).

In the western mouth of the Tsugaru Strait, such a seasonal mode has not been reported. However, the flow field associated with the TWC dynamically changes in response to the bathymetry of the Tsugaru Strait, whose topography is rugged (Fig. 1b). Ida et al. (2016) investigated the inflow pathway of water from the Sea of Japan into the Tsugaru Strait, finding this pathway to be highly sensitive to local bottom topography. A sill runs across the narrow part of the strait at 140.3ºE, as indicated by 200 m contours in Fig. 1b. Focusing on this sill where the depth is only 120 m compared to the 250 m background seafloor depth, Ohta et al. (2015) investigated the temporal evolution of internal waves arrested leeward of the sill, which are amplified depending on the speed of tidal currents over the sill. This sill corresponds to the nodes of diurnal tidal currents, according to a two-dimensional numerical model by Isoda and Baba (1998). Furthermore, Iino et al. (2009) implied that the SLD between the Sea of Japan side and the Pacific side, which is the main driving force of the TWC, is maintained by form drag associated with rugged topography rather than by bottom friction.

In the eastern mouth of the strait, there is a finger of land that extends to the north: Cape Shiriyazaki (Fig. 1b). As an extension of this terrestrial topography, an underwater plateau extends to the north for 30 km with a maximum width of 20 km and with depths of <100 m along the ridge of the plateau, i.e., elevated approximately 200 m above the background seafloor (Fig. 1b). This topography would be expected to influence the pathway and current speed of the TWC, but this impact has been little studied.

In addition, seasonal outflow modes, i.e., Gyre and Coastal modes, are present in the east. The pathway of the TWC in this mouth would change accordingly. Rosa et al. (2007), who analyzed data from hydrographic surveys to investigate seasonal variations of water system in the confluent region of Oyashio, Coastal Oyashio, and Tsugaru Warm Current in the Southern area of Hokkaido island, refers to meridional migration of the TWC. However, detailed seasonal pathway of the TWC including the quantitative estimation as well as its relation to the topography off the Cape Shiriyazaki has not been made clear. Continuous monitoring of the current fields is required to conduct that study,

but heavy traffic by international and domestic vessels in this international strait and busy ferry activity prevents the in-situ based continuous monitoring such as mooring observation.

The Japan Agency for Marine–Earth Science and Technology (JAMSTEC) has deployed high-frequency ocean radars (HFRs) on both coasts of the strait and has monitored surface currents since 2014 (Fig. 1a). HFRs can observe current velocities only within 1 m of the sea surface (Barrick et al. 1977) and hence are easily influenced by surface winds (Paduan and Washburn 2013), but they have the advantage of continuously observing the velocity distribution over a wide area. Surface current monitoring by HFRs can reveal details regarding TWC seasonality and the TWC's response to bottom topography.

There are many reasons for conducting this study. If locally strong current is observed in the shallow seafloor region, this may cause a strong vertical mixing (e.g., Bering Strait (Abe et al. 2019)). In addition, this may be another spot of arresting internal wave in the lee of the sill, whose breakup can be another process of causing vertical mixing. No needless to say, this physical process is important for nutrient upwelling and the supply of near-bottom materials to the surface that supports biological production. Further, this knowledge is important for safer marine navigation for vessels in the international strait as well.

Therefore, here we use HFR data to investigate the spatio-temporal variation of the TWC at the eastern mouth of the Tsugaru Strait. Objective of the present study is to reveal seasonal pathway of the TWC and its response to bottom topography. Special focus is placed on seasonal pathways of the TWC and on the TWC's response to bottom topography. The present paper is organized as follows. Section 2 describes the data and processing. Section 3 presents seasonal variation of the HFR surface current field, seasonal pathways, and current velocities of the TWC to relate them to SLDs and bottom topography. Section 4 discusses the impact of topography on TWC current velocities and dynamics of north/south shift of the TWC. Section 5 presents a summary.

2 Data and definitions

2.1 HFR surface velocity data

Three HFR systems were installed on the eastern coasts of the Tsugaru Strait in April 2014 (Fig. 1a): Ohata (41.44°N, 141.13°E), Iwaya (41.39°N, 141.41°E), and Esan (41.74°N, 141.08°E). A SeaSonde HFR system manufactured by CODAR OCEAN SENSORS LTD. was employed in each case (Barrick et al. 1977; Barrick and Lipa 1997). The radar systems were installed inside of fishery buildings at

Iwaya and Esan stations but mounted on a fishing port at Ohata station. The three HFRs on the Tsugaru Strait operated at a frequency of 13.9 MHz. The radial coverage was a maximum of 60 km with 3 km range cell resolution and 5° angular resolution. The radial component of current velocity was obtained every 4 min. Vector-form velocities were calculated at overlap areas of two of HFR coverage areas. A vector-type velocity averaged over 75 min was obtained every 30 min. The depth of the flow velocity detected by the radar was about 1 m (Barrick et al. 1977). Accuracy of HFR surface currents in vector form was better than 0.20 m s^{-1} for both eastward and northward components based on an analysis conducted in the Soya Strait (Ebuchi et al. 2006), and 0.0662–0.113 m s^{-1} for the radial component based on an analysis conducted in the Tsushima Strait (Yoshikawa et al. 2006). Our comparison of the HFR surface currents with moored current meter at 3 m-depth, drifting buoy with drogue attached at 15 m depth, 30 m-depth ADCP data indicated root mean square difference of 0.28 and 0.19 m s^{-1}, 0.19 and 0.14 m s^{-1} (not shown), 0.30 and 0.26 m s^{-1} (Abe et al. 2020) for zonal and meridional components, respectively.

The HFR velocity data were output at latitude and longitude grid intervals of about 3×3 km. These data were repositioned on a 0.01° × 0.01° grid (latitude × longitude), and a 1–2-1 filter was applied three times over. The analysis period was from April 1, 2014, to March 31, 2020.

Among the three HFR stations, Esan station experienced unexpected system shutdown five times (June 25–July 25, 2014; July 14, 2015–February 15, 2016; December 15, 2016–January 27, 2017; February 10–17, 2017; March 10–13, 2017), Iwaya station one time (August 1–30, 2019), and Ohata station one time (October 9, 2019–July 7, 2020) due to extreme instrument temperatures, antenna failure, and other minor troubles. These outages temporarily reduced velocity coverage and degraded the overall quality of the data.

To remove the high-frequency signal of strong tidal currents (Kuroda et al. 2004) from HFR data, a 25-h running mean filter was applied to the 30-min surface current vectors in each grid cell, after which daily-mean current fields were calculated. This data process follows the method used by Ebuchi et al. (2006). A 48-h tide-killer filter (Thompson 1983), eliminating tidal variation more precisely, was not utilized because there were several gaps in the surface current data, as described by Ebuchi et al. (2006) for their analysis of HFR current data for the Soya Warm Current.

2.2 Ship observation data

Data collected also included temperature and salinity (T–S) as measured by Conductivity Temperature and Depth profiler (CTD, SBE 19plus, SeaBird Electronics, Inc.) onboard

Hokkaido University's training ships *Ushio-Maru* and *Oshoro-Maru* (http://ships.fish.hokudai.ac.jp/en/). JAMSTEC's Mutsu Institute for Oceanography, together with the Faculty of Fisheries Sciences at Hokkaido University, has monitored the physical and biochemical properties of the waters of the Tsugaru Strait along the Shiriyazaki–Esan line (SE-line, Fig. 1b) quarterly since 2009. The SE-line consists of nine hydrographic stations ranging from the southernmost station SE01 (41.46ºN and 141.4ºE) to the northernmost station SE09 (41.82ºN and 141.22ºE). Table 1 summarizes information on cruises carried out on the SE-line. CTD data were obtained from the sea surface to a depth 10 m short of the seafloor. Raw CTD data were bin-averaged into 1-dbar intervals, where 1 dbar = 10 kPa. T–S profiles were used to calculate geostrophic current velocity normal to the SE-line. The no-motion level was set to 150 dbar for the stations whose deepest layer exceeded 150 dbar (SE03–08), while no such calculation was done for stations shallower than 150 dbar. Vessel-mounted ADCPs on *Oshoro-Maru* (75 kHz phased array ADCP, Teledyne RD Instruments) were used to examine subsurface velocity structure. The configuration of the ADCP measurement was set such that the first bin depth was 16 m and the vertical resolution was 8 m. We used data from the 6th bin, centered at a depth of 52 m, since data obtained near the body of the ship would be unreliable. One-minute averages of ADCP data were used. ADCP observation across the sill off Cape Shiriyazaki was conducted on February 25, 2019. This data, along with the following drifting buoy data, is used to examine response of TWC to sill topography.

2.3 Drifting buoy data

Lagrangian velocity can be estimated using the trajectory of a drifting buoy. We used one ARGOS buoy manufactured by Nomad Science (http://www.nomadsci.com/). The buoy has a diameter of 0.55 m, a height of 0.15 m, and a drogue 1.4 m long. We adjusted a length of rope so that the center of the drogue was positioned 15 m below the sea surface. In order to measure the Lagrangian velocity of the TWC, we performed 4 h of drifting buoy measurement starting at 23:00 JST on November 10, 2019, during an *Ushio-Maru* cruise. We focused on changes in TWC current velocity related to changes in depth off Cape Shiriyazaki. Before buoy deployment, we carefully checked near-real-time HFR current maps so that the drifting buoy would not miss the main stream of the TWC. The position of the drifting buoy was tracked by Global Positioning System, and position information was transmitted to the ARGOS satellite system. The sampling interval was about 15 min. The Lagrangian velocity was calculated based on a finite difference scheme using the locations of the two adjacent points, and the calculated midpoint velocity was output.

2.4 Sea level data

Hourly sea level data measured at two coastal tide-gauge stations, Fukaura and Hakodate (Fig. 1a), were provided by the Japan Meteorological Agency (JMA). SLD between Fukaura and Hakodate have been widely recognized as an indicator of TWC volume transport (e.g., Nishida et al. 2003). Some studies use sea level data at Hachinohe and Fukaura to relate them with TWC volume transport (e.g., Ito et al. 2003). Currently, no observed SLD in Hachinohe are provided by JMA because the tide gauge station suffered severe damage from huge tsunami caused by 2011 Japan earthquake. We instead obtained hourly sea level data at Hachinohe port provided by Sendai Research and Engineering Office for Port and Airport, Tohoku Regional Development Bureau, Ministry of Land, Infrastructure, Transport and Tourism. Data at Fukaura and Hakodate are mainly used in the present study, while data at Hachinohe port (hereafter called as "Hachinohe") are presented only in Discussion. Same data processing has been performed to all the three hourly data as follows. We selected mean sea level of Tokyo Bay (T.P.) as the baseline for the sea level data to avoid the influence of local

Table 1 Hydrographic observations performed by training ships *Ushio-Maru* (U) and *Oshoro-Maru* (O) on a hydrographic transect of the Shiriyazaki–Esan line during the period of January 2009 to December 2018

Season	Winter			Spring			Summer			Autumn		
Year Month	J	F	M	A	M	J	J	A	S	O	N	D
2009											U	
2010		U			U			U			U	
2011		O			U		U				U	
2012		U				U		U			U	
2013					U			U				
2014		U						U			U	
2015		U	U		U						U	
2016		U			U	U					U	
2017					U							
2018		U										

crustal movement. A 25-h running mean filter, the same filter used for the HFR data, was applied to these hourly sea level data to remove tidal signals. After averaging them into daily data, atmospheric pressure correction was conducted using daily-mean sea level pressure observed at each tide-gauge station (https://www.data.jma.go.jp/gmd/risk/obsdl/index.php).

2.5 Wind data

We downloaded operational weather forecasting 12-h wind data at a 10-m height output from the grid point value mesoscale model (GPV–MSM) provided by the JMA. The horizontal resolution was 0.05°×0.0625°. These data were used to remove wind-driven current effects from the HFR surface current data. After averaging the wind data into daily data, the wind-driven current was calculated using the speed factor α (ratio between the magnitudes of the wind drift current and the wind speed) and turning angle θ (difference between the directions of the wind and wind drift current)

by referencing the Soya Strait result (Zhang et al. 2016). To remove the wind-driven current, the calculated daily-mean wind-driven current was subtracted from the daily-mean HFR surface current.

3 Results

3.1 Seasonal pathway of the TWC

Figure 2 shows long-term monthly mean HFR surface current fields in the eastern mouth of the Tsugaru Strait. The spring, summer, autumn, and winter seasons cover the months April–June, July–September, October–December, and January–March, respectively. The TWC, an eastward current flowing into the North Pacific Ocean from the Sea of Japan, was clearly evident in every month and season. The current speed changed seasonally: relatively stronger during the summer and autumn and weaker during the winter and spring seasons. Furthermore, our visual inspection of Fig. 2
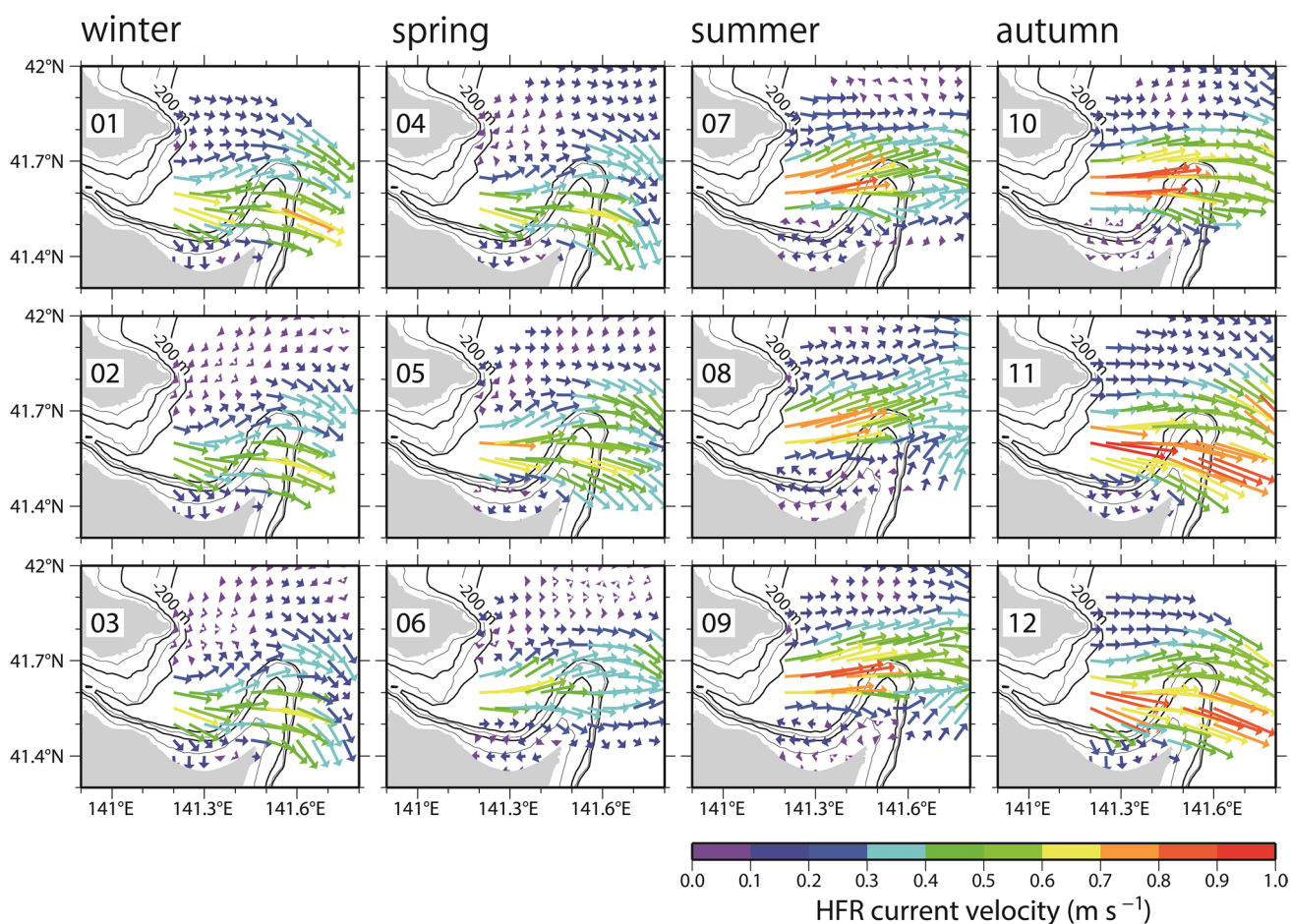
Fig. 2 Long-term monthly mean map of high-frequency ocean radar-based surface current velocity as averaged during the period of April 2014 to March 2020. The background contours indicate seafloor depth (m)

indicated that the TWC pathway shifted meridionally, with a northward shift in the summer season and a southward shift in the winter season. During the northward shift, an anticyclonic circulation emerged in the southern flank of the TWC (41.4°–41.6°N and 141.2°–141.4°E). The current speed changed along the TWC pathway as well. In the summer season, the maximum current speed was found in the center of the eastern mouth of the strait at around 141.3°E. Two peaks were clearly detected in the winter season and season before/after the winter (from November to May); one peak was at around 41.5°N and 141.3°E, another peak was off Cape Shiriyazaki at 41.5°N and 141.5°E. In November, the third peak emerges further offshore at 41.7°N and 141.8°E.

The meridional position of the TWC was examined using HFR surface current data (Fig. 3). The TWC axis was the set of points each defined as the latitude of the daily-mean maximum current velocity for a given longitude. By connecting the latitudes that were determined as the location of the TWC axis at each longitude, we can create a map showing the spatial pattern of the TWC axis as a broken curve. This method works effectively as long as the TWC flows

eastward. Figure 3 shows the long-term monthly mean of the TWC axis calculated using daily-mean data with the standard deviation of the daily-mean value within each month. A comparison of the axis position across the four seasons indicated that the TWC axis shifted northward in summer and southward in winter. Spring and autumn are the transition seasons. The summer path was located at northern edge of the sill where bathymetry contours are crowded, while the winter path crossed the core of the sill.

The latitude of the TWC axis estimated before entering into the sill (141.3°E) was maximum in August (41.64° ± 0.05°N) and minimum in February (41.55° ± 0.04°N); this 0.09° seasonal shift was statistically significant ($p < 0.05$), whose statistical test is based on a two-sample t-test assuming that the daily mean latitude of the TWC axis for August, when the pathway is at northernmost, and February, when it is at southernmost, do not have equal variances.

Figure 4a and b show that as indicated by circle symbols, warm saline TWW occupied the waters 20–40 km from the southern coast throughout the year, while during winter
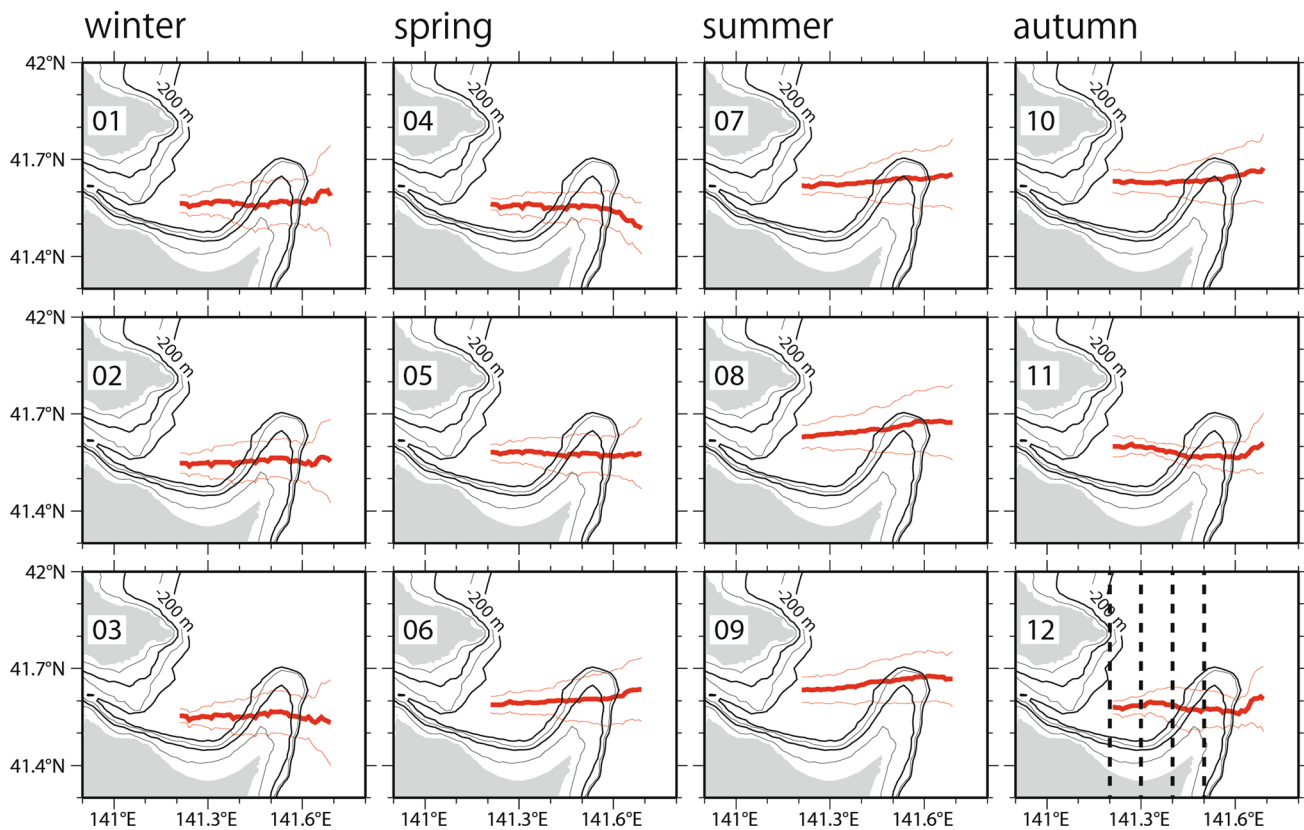
Fig. 3 Long-term monthly mean map for axis of Tsugaru Warm Current (thick red line) calculated using daily-mean values as averaged during the period of April 2014 to March 2020. The axis was defined as the latitude of the maximum current velocity at each longitude. Thin red lines on both sides of the thick red line denote standard

deviation of the daily-mean high-frequency ocean radar-based surface currents. Background contours indicate seafloor depth (m). Four longitudes at which the current velocity of the Tsugaru Warm Current was examined are shown in panel of December as dashed line: Line 1 (141.2°E), Line 2 (141.3°E), Line 3 (141.4°E), and Line 4 (141.5°E)
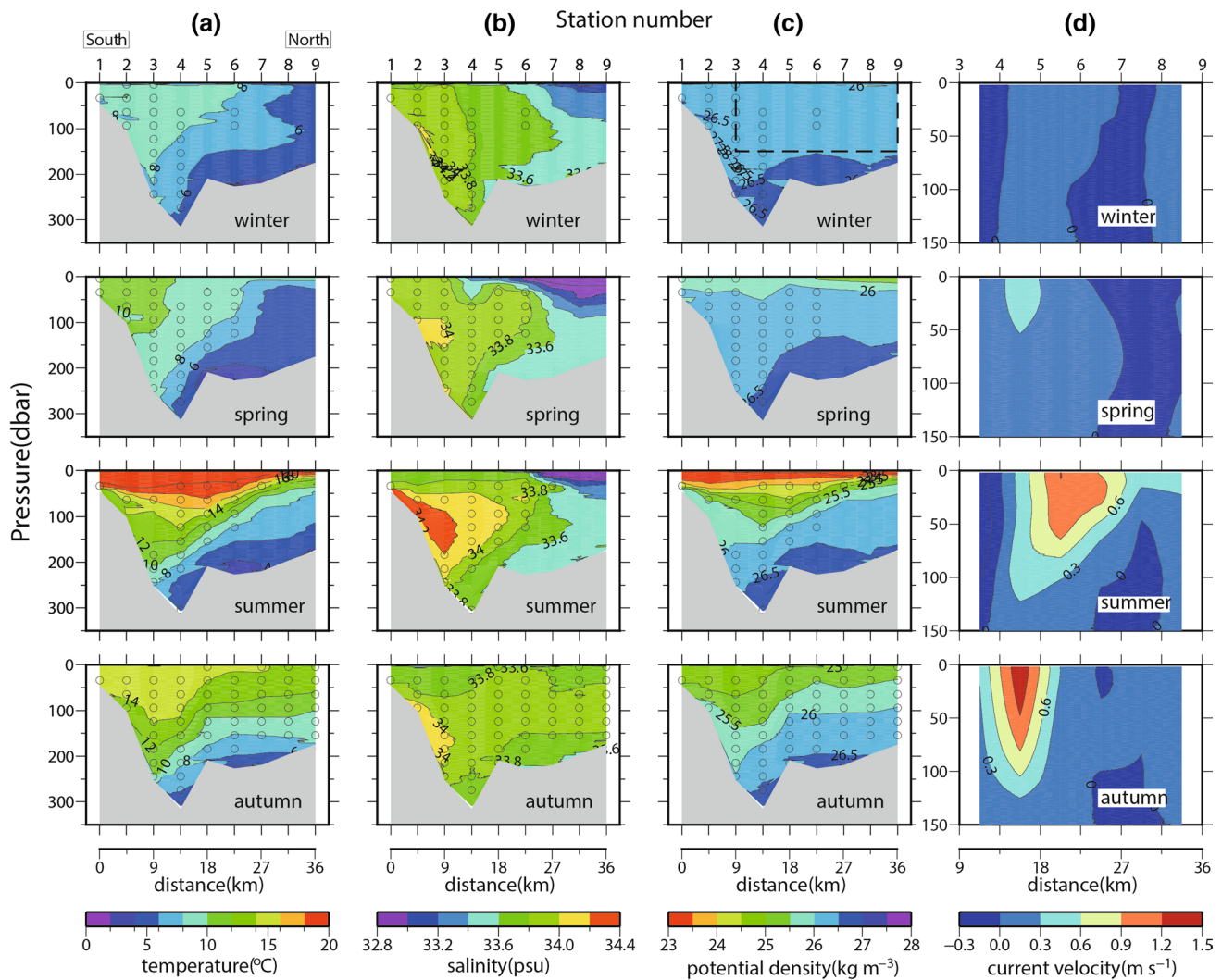
Fig. 4 Vertical section of seasonally averaged **a** temperature (ºC), **b** salinity, **c** potential density (kg m⁻³), and **d** baroclinic geostrophic current velocity referenced on a no-motion level of 150 dbar along a hydrographic transect of the Shiriyazaki–Esan line. Contour intervals are **a** 2 °C, **b** 0.2 psu, **c** 0.5 kg m⁻³, and **d** 0.3 m s⁻¹. Tsugaru Warm Water detected is highlighted by circles at 30 dbar intervals (no detection for Coastal Oyashio Water). Dimensions of **d** represent a zoomed-in view of the box marked in (**c**). In (**d**), positive values for velocity indicate an eastward current

season, cold water with a fresher salinity of less than 33.0 dominated from the surface to a depth of 20 m in waters 10–20 km off the northern coast. This fresher water seems to reflect the influence of the COW (Shimizu et al. 2001), although this water mass does not strictly satisfy the definition of COW (Hanawa and Mitsudera 1987).

The vertical section of potential density (Fig. 4c) shows the contrast between lighter water formed in the south and denser water formed in the north. This meridional contrast was evident in summer and autumn seasons and found in spring season during which the density front reached as deep as 50–200 dbar, while in winter the density contrast vanished across the section irrespective of the presence of distinct

meridional contrasts in temperature (Fig. 4a) and salinity (Fig. 4b).

Consequently, except for winter season, a baroclinic current emerged, flowing eastward. Especially in autumn season, this geostrophic flow in the surface exceeded a speed of 1.00 m s⁻¹ at maximum, although this is not same as HFR surface current that includes barotropic and baroclinic geostrophic components and ageostrophic component (Fig. 2). Furthermore, a comparison of the meridional position of the baroclinic flow across these three seasons indicated that the maximum current speed in summer was positioned at a northern site relative to that in spring and autumn seasons. Essentially no baroclinic flow was apparent in winter season.

## 3.2 Relationship between sea level difference and HFR surface current

The current velocity of the TWC was estimated at four different longitudes: 141.2ºE, 141.3ºE, 141.4ºE, and 141.5ºE, hereafter called Line 1, Line 2, Line 3, and Line 4, respectively (Fig. 3). We defined each Line's TWC current velocity as the maximum current velocity observed at that longitude. The reason why not using the averaged current velocity over the width of strait is low signal-to-noise (S/N) ratio for potential correction error for wind-driven current; averaged velocity is smaller than maximum velocity,

hence the S/N ratio becomes low for a certain amount of potential error. Figure 5a–d shows a time series of monthly-mean TWC velocities at each of the four longitudes for the analysis period. The TWC exhibited variability at intraseasonal, seasonal, and interannual timescales. A statistically significant seasonal variability was detected by spectral analysis (Fig. 6). As an example, analysis of the daily-mean time series on Line 2 demonstrated that the one-year cycle showed the largest value, significantly larger than the fluctuations pertaining to longer and shorter periods. The long-term monthly-mean value was superposed on each panel of Fig. 5 for a clear representation of the seasonal

Fig. 5 Time series of monthly-mean current velocity of Tsugaru Warm Current based on daily-mean high-frequency ocean radar-based surface currents at **a** Line 1 (141.2ºE), **b** Line 2 (141.3ºE), **c** Line 3 (141.4ºE), and **d** Line 4 (141.5ºE). Current velocity of the TWC was defined as the maximum current velocity at each longitude. **e** Sea level difference between two tide-gauge stations (Fukaura minus Hakodate). Vertical bars denote standard deviation of daily-mean value within each month. Long-term monthly mean as averaged during the period of April 2014 to March 2020 is shown as a gray line
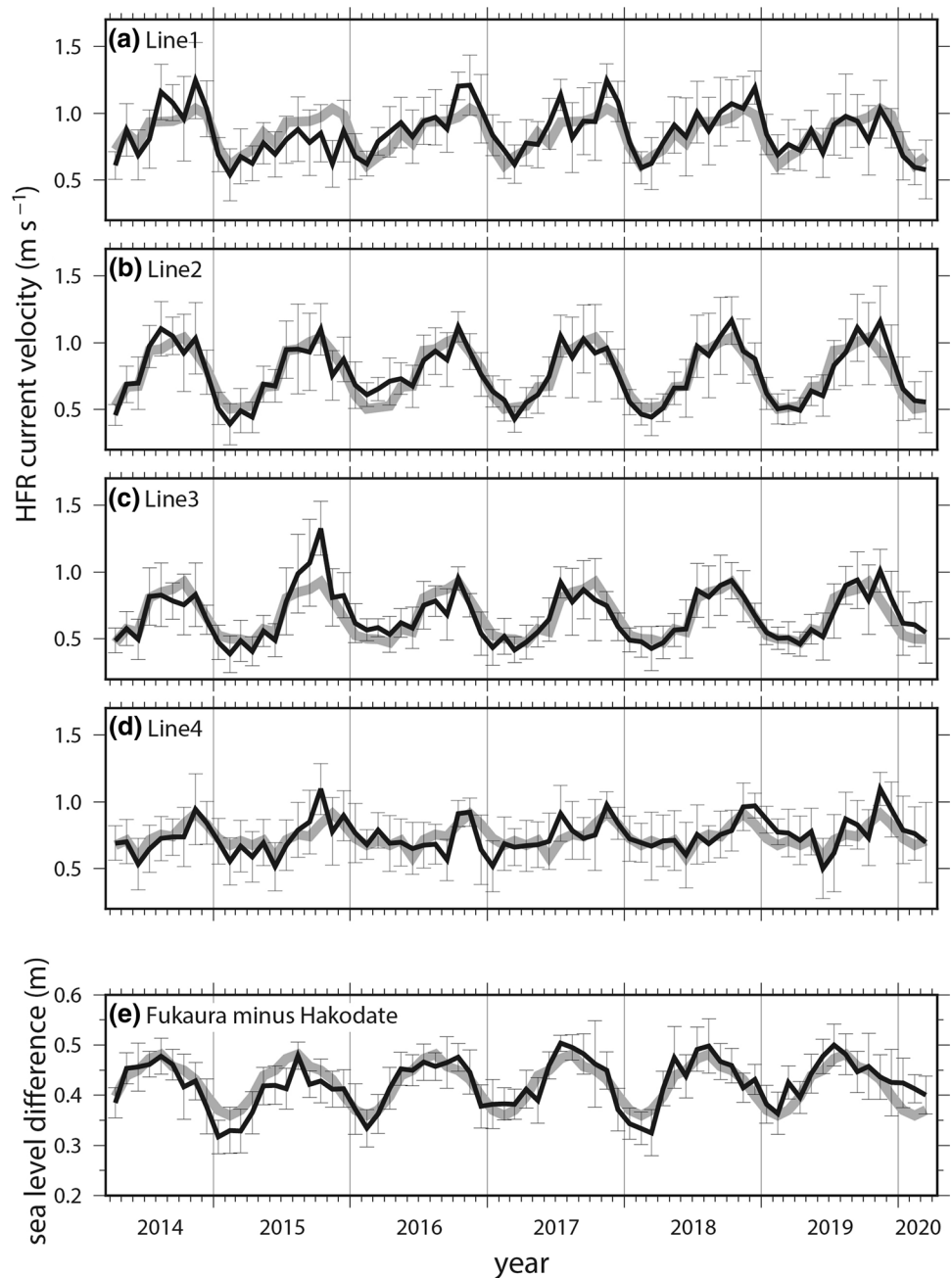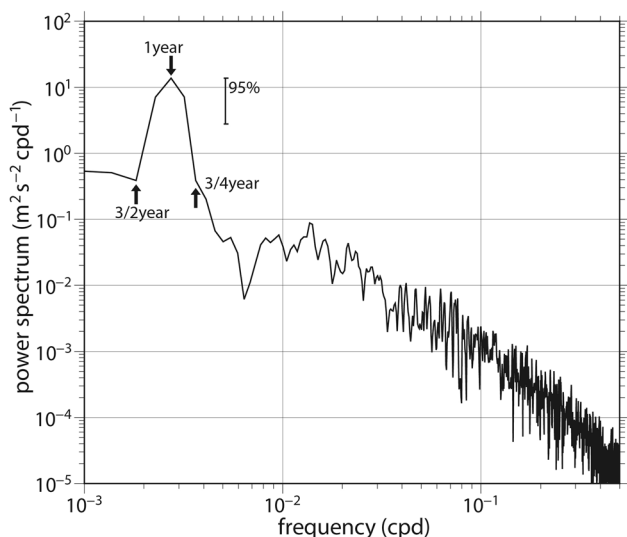
Fig. 6 Power spectrum density (m^2 s^{-2} cpd^{-1}) of daily-mean current velocity of Tsugaru Warm Current using daily-mean high-frequency ocean radar-based surface currents at Line 2 (141.3° E). Vertical bar denotes 95% significance level

cycle. The long-term monthly-mean time series on Line 1 (Fig. 5a) and Line 2 (Fig. 5b) tended to exhibit strong current velocity in summer and autumn (~ 1.00 m s^{-1}) while weak in winter (~ 0.50 m s^{-1}). This seasonality was evident on Line 3 as well, although the seasonal range shifted slightly toward weaker velocity values (Fig. 5c). On Line 4 (Fig. 5d), seasonality was unclear with the maximum value being small and the minimum value being large compared to those of other Lines. The time series of SLDs between Fukaura and Hakodate (Fig. 5e) was generally in phase with that of Line 1–3. These two time series were compared as scatter plot with SLD on the X-axis for and current velocity

on the Y-axis (Fig. 7). A significant positive correlation was observed for each of Line 1 ($r = 0.53$, $p < 0.05$), Line 2 ($r = 0.68$, $p < 0.05$), and Line 3 ($r = 0.59$, $p < 0.05$), suggesting that the seasonality of TWC current velocity would be related to SLD between the two oceanic basins. This result, based on HFR in the eastern mouth of the strait, is consistent with results from Nishida et al. (2003), which used ship-board ADCP to demonstrate seasonal variability in TWC transport in the western mouth of the Tsugaru Strait. On Line 4, however, the correlation was poor ($r = 0.14$) and not statistically significant ($p > 0.05$). SLD between Fukaura and Hakodate as the mechanism for seasonal variability of the TWC does not hold for TWC velocity on Line 4.

3.3 Gyre mode and Coastal mode: topographic effect

The seasonal surface current map in Fig. 2, along with the time series analyses in Fig. 5, indicate that only during Coastal mode does the TWC seem to intensify off Cape Shiriyazaki, where the seafloor is elevated by 200 m above the surrounding seafloor. Coastal mode was typically observed in winter although this could be observed in autumn and spring seasons as well (Fig. 2). To examine this topographic effect, hydrographic surveys were carried out using a ship-board ADCP and a drifting buoy. A snapshot of 1-min mean current velocity at a depth of 52 m by ship-board ADCP on February 25, 2019, when the TWC was in Coastal mode (Fig. 8) indicated that current velocity reached its maximum at the shallowest part of the sill. The current velocity (1.00 m s^{-1}) observed over the shallow seafloor (< 100 m) was intense compared to that (0.60 m s^{-1}) observed over the deep seafloor (300 m).
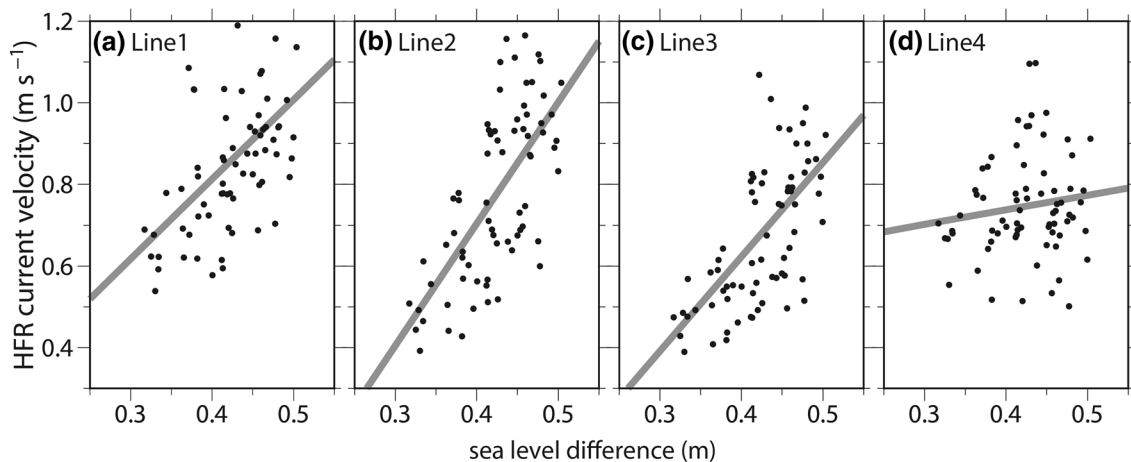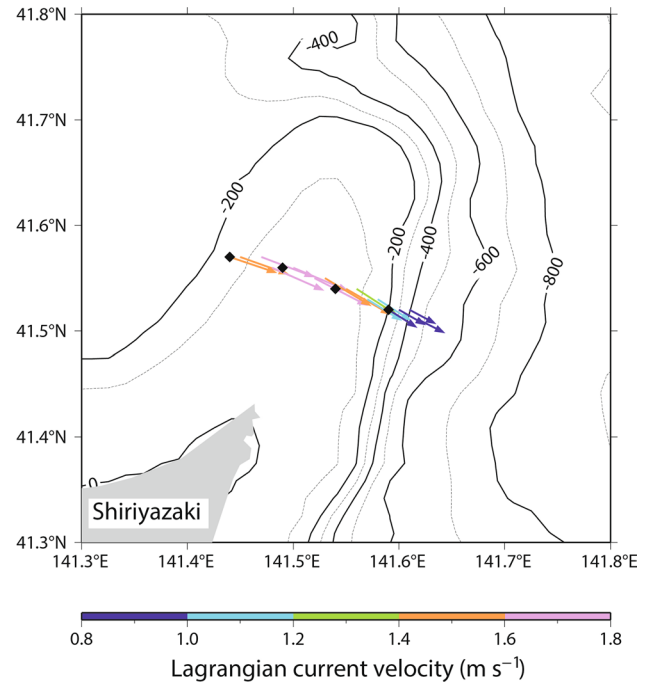

Fig. 7 Scatter plots of monthly-mean high-frequency ocean radar-based current velocity of Tsugaru Warm Current versus sea level difference between two tidal stations (Fukaura minus Hakodate) with linear regressions for **a** Line 1 (141.2°E), **b** Line 2 (141.3°E), **c** Line 3 (141.4°E), and **d** Line 4 (141.5°E)
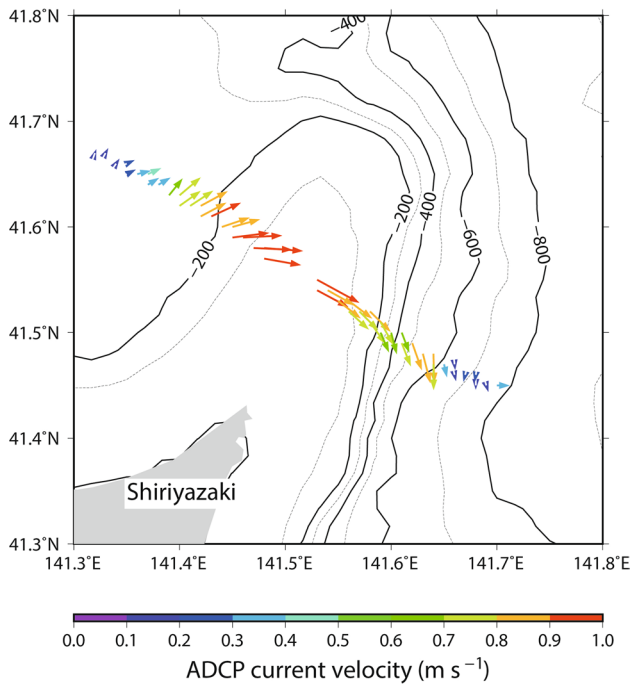
Fig. 8 Snapshot of 1-min mean current velocity observed by shipboard acoustic Doppler current profiler at a depth of 52 m along the transect of the training ship *Oshoro-Maru*'s cruise off Cape Shiriyazaki during the period 19:40–21:40 (JST: Japan Standard Time) on February 25, 2019. The velocity data of percent good less than 90% were removed. The background contours indicate seafloor depth (m)

Fig. 9 Snapshot of Lagrangian velocity estimated using 15-min mean trajectory of 15-m drogue-attached drifting buoy off Cape Shiriyazaki from 23:00 JST (Japan Standard Time) on November 10, 2019, to 03:00 JST on November 11, 2019. The Lagrangian velocity is calculated based on a finite difference scheme outputted at the geographic midpoint of each pair of adjacent points. The background contours indicate seafloor depth (m). Black square symbols indicate selected high-frequency ocean radar grids where temporal variability of 30-min surface current was examined during this 4-h experiment as shown in Fig. 11

Attention is required in interpreting this ADCP current map because the TWC pathway was not the perfectly straight line like the ADCP transect (not shown). Change in the surface current along the transect does not represent change along the TWC pathway in a strict sense. Thus, we performed a drifting buoy experiment that could capture the change along the TWC pathway in the different cruise on November 10, 2019. Figure 9 shows the Lagrangian velocity along the trajectory of the buoy that drifted from upstream to downstream of the sill. The observed velocity was 1.70 m s^{-1} at the shallowest bottom depth (< 100 m), which was higher than the velocities in the upstream and downstream regions of the sill. Indeed, the velocity of the drifting buoy showed a negative relationship with bottom depth (slope: -0.00219 m s^{-1} m^{-1}; Fig. 10), with a correlation coefficient of -0.56 ($p < 0.05$). Tidal currents may have influenced these results to some extent. We used HFR current velocity to show temporal variability of the TWC along its pathway upstream of the sill (41.57ºN and 141.44ºE), on the sill (41.56ºN and 141.49ºE), downstream of the sill (41.54ºN and 141.54ºE), and further downstream (41.52ºN and 141.59ºE) during the four-hour drifting buoy experiment (Fig. 11). Tidal currents are included in these HFR data at intervals of 30 min. Although temporal variability was found, a comparison of the current velocity across the three

grids indicates that surface current velocity in the second grid (approximately 1.40 m s^{-1}), where bottom depth was shallowest among the four grids, was always stronger than in the other grids. Likewise, at the fourth grid where the seafloor depth was deeper than the other grids, the current velocity was always smaller than those in the other shallower grids. This result demonstrates the local intensification of TWC by sill topography in the presence of tidal currents.

4 Discussion

4.1 Effect of bottom topography

A localized spot of TWC intensification associated with bottom topography was detected only in Coastal mode. A linear regression line in Fig. 10 (Y = $-0.0022X + 1.6918$) indicates that the current velocity along the TWC pathway increased from 1.3 to 1.6 m s^{-1} as it flowed from the deeper seafloor region (170 m) to the shallower seafloor region (60 m).

According to Pratt and Lundberg (1991), once a steady state has been established it is possible to relate the

Fig. 10 Scatter plot with linear regression for buoy-based Lagrangian velocity of Tsugaru Warm Current (see Fig. 9) versus seafloor depth off Cape Shiriyazaki
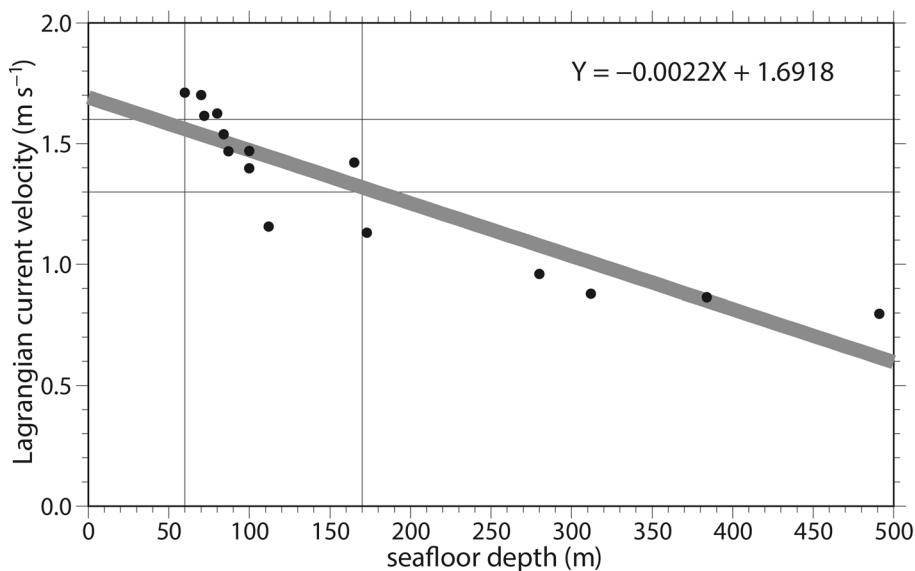
Fig. 11 **a** Temporal variability of TWC upstream of the sill (41.57ºN and 141.44ºE), on the sill (41.56ºN and 141.49ºE), and downstream of the sill (41.54ºN and 141.54ºE), and further downstream (41.52ºN and 141.59ºE) for a drifting buoy experiment performed during a cruise of the training ship *Ushio-Maru*. See Fig. 9 for location. 30-min high-frequency ocean radar-based surface current velocity data without corrections for tide and wind-driven currents were used. **b** Bottom topography along the buoy trajectory
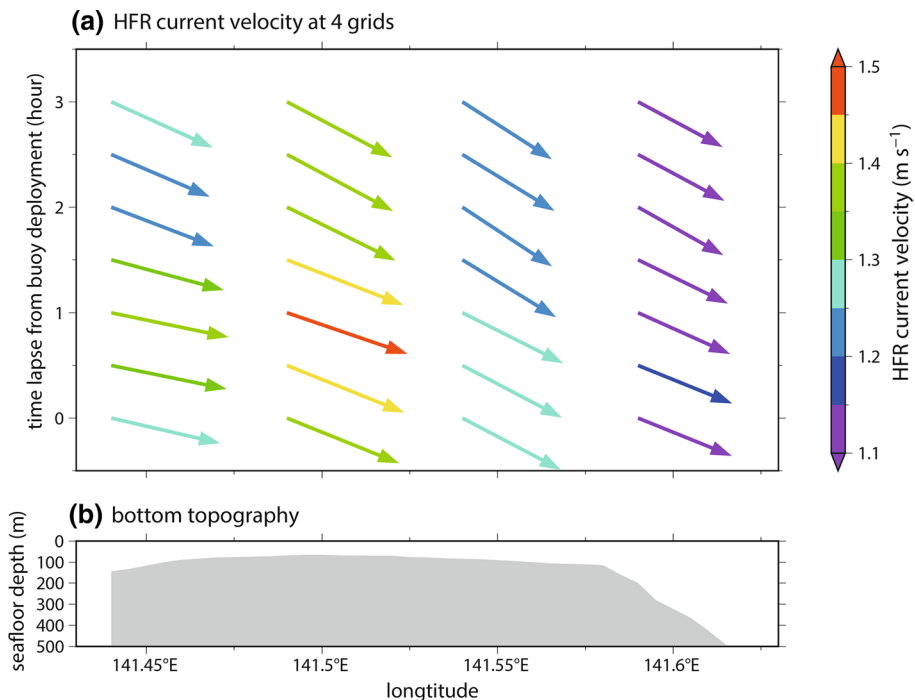
conditions at the sill to those upstream of the sill using the mass conservation. For a shallow, one-dimensional flow, the volume transport Q is conserved;

$$u\,h\,l = Q \tag{1}$$

where u, h, l denotes the horizontal velocity, depth, and the width of TWC, all of which vary with direction of TWC. If the sill and upstream are distinguished by subscript notation "s" and "u", the mass conservation $Q_u = Q_s$ yields

$$u_u h_u l_u = u_s h_s l_s \tag{2}$$

or

$$u_s = (h_u/h_s)\,(l_u/l_s)\,u_u \tag{3}$$

For the case of l being constant, this equation is further simplified as follows;

$$u_s = (h_u/h_s)\, u_u \tag{4}$$

Here, we apply this Eq. (4) to the TWC in the eastern mouth of the strait, where it qualitatively explains the intensification of the TWC over the shallower seafloor. The observed intensification ratio ($1.6/1.3 = 1.2$), however, does not reach the level predicted by this simple Equation. ($170/60 = 2.8$). This discrepancy could be due to various invalid assumptions. The assumption of barotropic flow is valid here, since we confirmed using the ADCP data that the flow in the subsurface exhibited barotropic structure in Coastal mode (not shown). However, an assumption of a horizonal one-dimensional channel may not be strictly satisfied in the actual TWC in the eastern mouth of the Tsugaru Strait.

According to Eq. (3) that permits changes in TWC width, l of the TWC at the sill has to increase by a factor of 2.3 if we apply the observed values of $u_s/u_u = 1.2$ and $h_u/h_s = 2.8$. Figure 12 shows four-hour mean of HFR-based current velocity field during when the drifting buoy experiment was performed (tidal and wind-driven currents uncorrected). Here the TWC current speed is expressed as colored
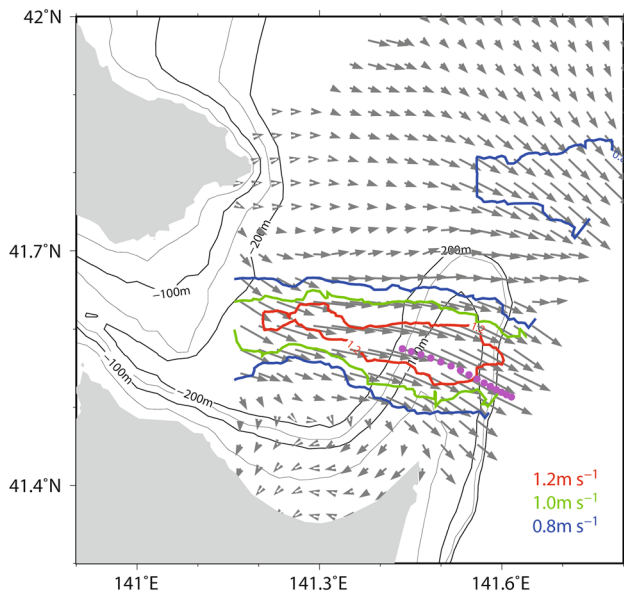
Fig. 12 Temporal average of 30-min high-frequency ocean radar-based surface current velocity averaged during four hours of a drifting buoy experiment from 23:00 JST (Japan Standard Time) on November 10, 2019, to 03:00 JST on November 11, 2019. 30-min high-frequency ocean radar-based surface current velocity data without corrections for tide and wind-driven currents were used. Current speed is expressed as colored contours: 1.2 m s^{-1} (red), 1.0 m s^{-1} (green), and 0.8 m s^{-1} (blue). Buoy trajectories are shown as well (magenta). The background contours indicate seafloor depth (m)

contours: 1.2 m s^{-1} (red), 1.0 m s^{-1} (green), and 0.8 m s^{-1} (blue). In addition to intensifying, the TWC widened meridionally over the sill crest. TWC width, defined as the span within the 1.2 m s^{-1} (red) contour, increased by a factor of 1.5 over the sill. This factor is 1.1 for TWC width defined by contours of 1.0 m s^{-1} and 0.8 m s^{-1}. These results indicate that widening of the TWC ($l_s/l_u = 1.1$–1.5) is comparable to an increase of the current velocity of the TWC ($u_s/u_u = 1.2$).

A combination of these two effects ($l_s u_s/l_u u_u$; 1.3–1.8), however, accounts for only 50–60% of the depth change in Eq. (3) (h_u/h_s; 2.8). The remainder is assignable to the assumptions made when deriving Eq. (3). In particular, the fundamental assumption of horizontal two-dimensionality may not be sufficient, i.e., part of the TWC may leak from the main flow. In the winter season, we often found locally strong flow off the northern tip of the sill at around 41.7ºN, 141.8ºE, as mentioned in Sect. 3.1 (see also Fig. 12). No evidence is yet available to bear on this point, but such a flow leak may partly account for the remainder of the depth change in Eq. (3). Further, a locally strong barotropic current (~ 1.00 m s^{-1}) at shallow seafloor depth (< 100 m) may cause strong vertical mixing that would be another leak factor.

4.2 Fluctuations in the TWC pathway during Coastal mode

Another question is why the TWC's Coastal mode takes a path across the sill rather than around the sill. Coastal mode is characterized by flow confined to a region near the coastline. This mode is typically seen in winter season when stratification is very weak (Fig. 4c). This confined flow continues downstream from Tsugaru Strait, where the TWC turns to the right to head south along the eastern coast (Conlon 1982). This means that the TWC could take the pathway around the sill if the elevation of the sill were high enough that the sill ridge mostly reached the sea surface. In contrast, the TWC is not disturbed if there is no sill with the seafloor being flat. The top of the sill is elevated 200 m above the background seafloor's depth of 300 m. The shape and height of the sill are fixed over time; instead, the TWC changes drastically on a seasonal timescale, indeed even intra-seasonally (Fig. 2). Given the fixed bathymetry, the flow strength of the TWC may be an important determinant of the pathway across or around the sill.

We now narrow our focus to Coastal mode, in which barotropic structure is exhibited. Figure 13 shows an example of Coastal mode in which the TWC pathway did not pass over the sill. At this time, the TWC was very weak (< 0.3 m s^{-1}), and a pathway around the sill was taken. The pathway of the TWC during Coastal mode may be sensitive to TWC speed upstream from the sill. This "upstream region" was selected as shown in Fig. 13 (41.50º–41.60ºN, 141.35º–141.45ºE).
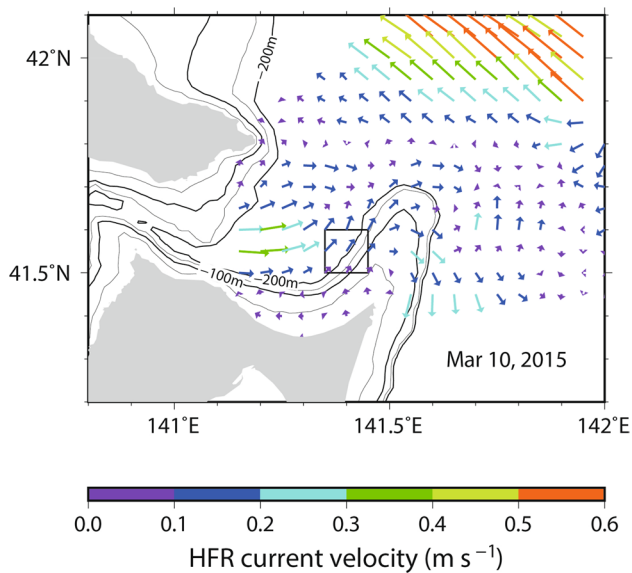
Fig. 13 An example of Coastal mode, in which the path does not cross the sill off Cape Shiriyazaki; data recorded March 10, 2015. Daily-mean high-frequency ocean radar-based surface current velocity is used (m s^{-1}). The background contours indicate seafloor depth (m). A box denotes the area defined as "upstream region" (41.5°–41.6°N and 141.35°–141.45°E) upstream of the sill over which the high-frequency ocean radar-based current velocity is averaged to show the time series in Figs. 14 and 15

Figure 14 shows the daily-mean HFR-based current velocity and inflow angle of the TWC upstream from the sill (41.5°–41.6°N, 141.35°–141.45°E) in the winter season. Here we defined inflow angle as the arctangent of (v/u), which is 0° for an eastward current and 90° for a northward current. On some occasions, the inflow angles, indicated by the black line in Fig. 14, assumed high values exceeding 45°; each such event lasted about a couple of days. In addition, this inflow angle tended to reach its local maximum when the current velocity (gray line in Fig. 14) reached its local minimum. In order to see this relationship in a clear way, we created a composite graph (Fig. 15). Figure 16 shows composite maps of daily-mean HFR-based current velocity for periods during which the inflow angle reached a local maximum exceeding 45°. Coastal mode took the usual across-sill pathway on Day −3 through −1, where day numbers are relative to the day of peak inflow angle (Day 0). Interestingly, as time passed, relatively strong current speeds exceeding 0.60 m s^{-1} gradually vanished from the current field of the TWC, while relatively weak current speeds below 0.30 m s^{-1} came to dominate. Current speed in this field was minimized on Day 0, when the direction of the TWC turned to the left to flow around the sill. Evolution of the current field after Day 0 mirrored that before Day 0. Figure 16 demonstrates that the around-sill pathway was observed when the TWC was weak for weak Coastal mode. A lack of sufficient momentum

to pass over the 200 m of seafloor relief may account for the around-sill path taken in weak Coastal mode.

The mechanism for causing occasional weakening of the current velocity during the Coastal mode has not been made clear. We have additionally analyzed CTD data to see interannual variability of wintertime T-S profiles after the deployment of HFR (Feb of 2015, 2016, 2018). Any year did not show evident density stratification in the south of TWC where occasional pathway shift of the Coastal mode occurs (not shown). This is unfavorable oceanic condition for propagation of internal wave, although this may not be true for outside of the strait where stratification is observed in the subsurface layer (e.g., Shimizu et al. (2001)). Weather data downloaded from website of Japan Meteorological Agency indicated that air temperature and wind observed at Oma (41.53°N and 140.91°E), the most northern tip of main island of Japan, did not show any characteristic tendency among the 10 events of the Coastal mode; air temperature was high on some events and low on other events, and same for wind speed and direction.

4.3 Dynamics of north/south shift of the axis

To our best knowledge, no published paper has reported north/south shift of the TWC in the eastern mouth of the Tsugaru Strait in detail, at least, in a quantitative manner. Dynamics of the Gyre and Coastal modes may be a key factor in understanding dynamics of seasonal meridional shift of the TWC. Let us introduce semi-permanent anticyclonic gyre in the Alboran Sea just east of the Strait of Gibraltar (Whitehead and Miller 1979), which is considered as similar gyre as Tsugaru Warm Gyre (Conlon 1982). Whitehead and Miller (1979) conducted a transient laboratory experiment on a rotating turntable using two basins connected by a narrow channel of the same depth. The main conclusion is that outflow jet behaves differently depending on internal Rossby radius of deformation, R_I. The outflow jet shows pronounced instability for relatively small R_I, but as R_I increases, the jet veers to the right, hugging the coast, and when R_I increased still further, the jet separates from the wall, and a return flow is generated at the separation point and a developed anticyclonic gyre is generated. Conlon (1982) discovered seasonal outflow modes of the Tsugaru Warm Current based on observation, whose occurrence is consistent with the laboratory finding of Whitehead and Miller (1979), which suggests that inertial-rotational dynamics govern the Tsugaru Warm Current.

Conlon (1982) also showed seasonal variability of R_I in Tsugaru Strait that ranges from 4.7 to 23.7 km, taking maximum value in August and September and minimum value in February and March. These months correspond to those of northward shift and southward shift, as mentioned in Sect. 3.1. Also, variability of R_I (= 19 km) is comparable

Fig. 14 Regionally averaged daily-mean high-frequency ocean radar-based current velocity (gray line) and inflow angle (black line) of TWC upstream of the sill (41.5°–41.6°N and 141.35°–141.45°E) in the winter season (January to March). Location of averaging region is shown in Fig. 13. Inflow angle was defined as the arctangent of (*v/u*), which is 0° for an eastward current and 90° for a northward current. Inflow angle peak values exceeding 45° are denoted by open square symbols. The data are not plotted for time points at which the TWC exhibited reverse flow
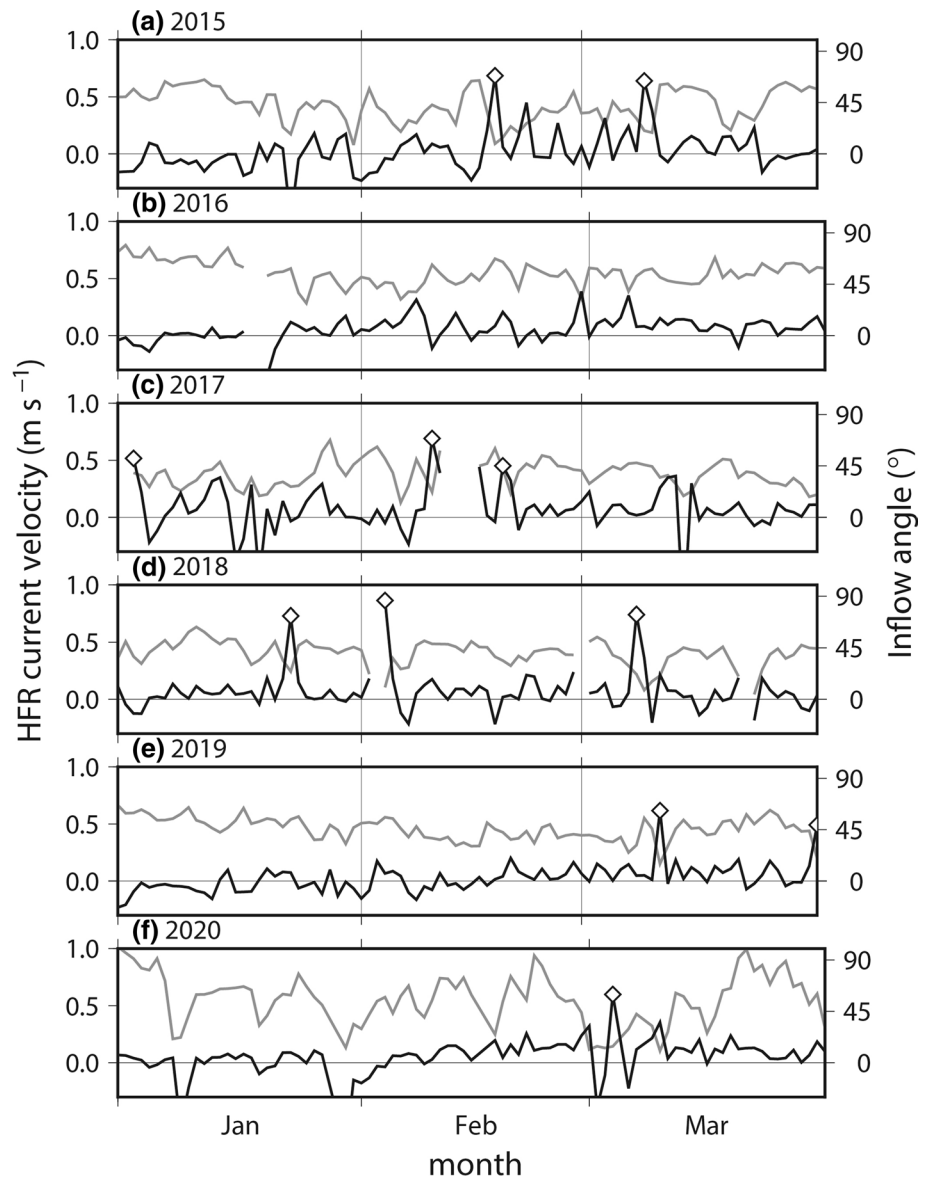
to the range of meridional shift (0.09° ≒ 9 km). These correspondences, however, do not immediately mean that dynamics characterized by the scale of R_I is the factor controlling the offshore scale of TWC. If the R_I is regarded as the offshore scale of the current trapped to the coast under the influence of Coriolis force like a coastal Kelvin wave, sea surface height (SSH) has to increase with shorter distance to the coast. This is not true as far as we see the HFR surface current map of Fig. 2, in which an anticyclonic circulation emerges in the eastern mouth of the Tsugaru Strait south of the TWC in summer only, and the presence indicates the SSH is not in maximum on the coast under the assumption of geostrophy.

Kubokawa (1991) proposed an idea to explain dynamics of the two seasonal outflow modes of TWC with focusing on low potential vorticity (PV). Front of TWC defined as

the boundary of two piecewise-uniform PVs with low PV along the southern coast, is investigated using a quasigeostrophic model. The simple model could successfully reproduce both the Gyre and Coastal modes. The limited capacity of the downstream coastal current to advect the low potential vorticity fluid and the characteristics of frontal waves are the main causes for the existence of these two modes (plus another coastal mode). The realistic current field measured by the HFR (Fig. 2) also shows weak westward flow in the south of the TWC axis (purple color), especially in summer season when anticyclonic circulation emerges (Kaneko et al. 2021), which would be low PV that Kubokawa (1991) focuses on. It can be considered that evolution of the anticyclonic circulation may be a forcing to push the TWC axis to the north. U-shaped boundary on the southern coast may play an important role in keeping the
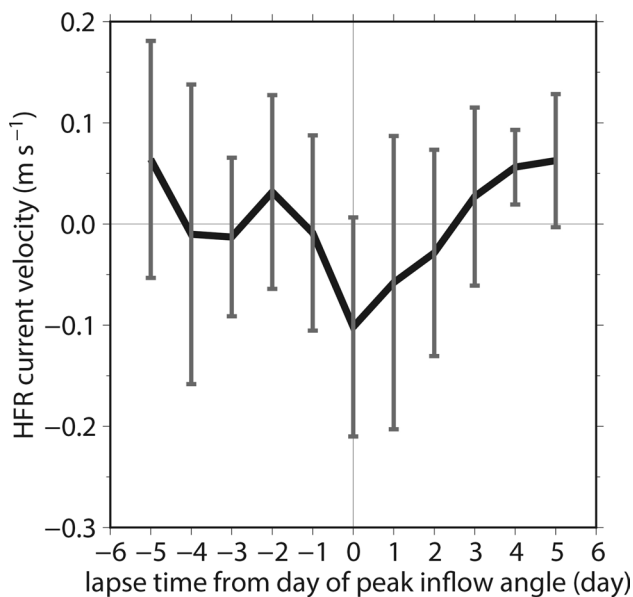
Fig. 15 Composite of daily-mean high-frequency ocean radar-based current velocity for periods during which inflow angle reached a local maximum exceeding 45º as calculated using data in Fig. 14. Data for 10 events (open square symbols in Fig. 14) are averaged here, producing mean values and standard deviations represented by black lines and vertical bars, respectively. Before calculating these statistical values, the temporal average during Day −6 to Day 6 was calculated for each event, after which was subtracted from the original daily-mean value

anticyclonic circulation, which has not been considered in a simple rectangular topography in Kubokawa (1991). Formation mechanism of the anticyclonic circulation still remains unclear. This may be a return flow of the intensified TWC in summer season.

4.4 Cross-strait and along-strait dynamic balance

SLD across the Tsugaru Strait (Fukaura minus Hakodate) enables us to calculate geostrophic flow on the assumption that planetary vorticity (or Coriolis parameter) f is large enough to neglect relative vorticity ζ, in which PV can be simplified as f/h. If this PV is conserved, then h has to be constant for the eastward flow without changing f. On the other hand, the HFR obviously revealed the flow crossing the sill topography. This suggests our assumption of geostrophic balance and/or constant f/h is not valid in a strict sense. In the winter season when the across-sill flow is observed, the assumption of $f >> \zeta$ cannot be applied because Rossby number is not enough to be negligible (about 0.4). Further, winter-time barotropic flow as the coastal mode is confined near the coast, which implies the flow is more or less influenced by bottom friction. These facts provide room for us not to apply strict condition as geostrophic balance and

conservation of PV, hence permits across-sill pathway and discussion using Eq. (1).

There are two proposed explanations on dynamic balance of the TWC; cross-strait SLD that balances with Coriolis force as geostrophic flow (Nishida et al. 2003), and along-strait SLD that balances with bottom friction (Ito et al. 2003; or form drag (Han et al. 2018)). We selected Fukaura and Hakodate to examine the cross-strait SLD, but it may be important to consider along-strait SLD, e.g., Fukaura and Hachinohe (see Fig. 1 for location of Hachinohe). Our calculation indicated that the along-strait SLD (Fukaura minus Hachinohe) shows a positive correlation coefficient with the TWC current velocity ($r = 0.21$), but this was much smaller than that obtained using cross-strait SLD ($r = 0.68$) at Line 2. The multiple regression, which considers both cross-strait and along-strait SLDs, shows increase of the coefficient ($r = 0.78$) from considering only the cross-strait SLD ($r = 0.68$).

The correlation coefficient may change depending on stratification. We calculated the coefficient for season of weak stratification and season of strong stratification. Winter and spring seasons are considered as the season of weak stratification, and summer and autumn seasons as the season of strong stratification. For both cases of cross-strait SLD and along-strait SLD, the correlations were higher in the weak stratification season ($r = 0.66$ and 0.53) than those in the strong stratification season ($r = 0.41$ and -0.06). In addition, correlations using the cross-strait SLD were higher than those using the along-strait SLD.

The balances for the across and along-strait SLDs may change seasonally or interannually. We identified relatively small SLD for both along-strait direction and cross-strait direction in March 10, 2015 (not shown) when the HFR current fields exhibited a pathway of the TWC around the sill as shown in Fig. 13. This does not mean that such small SLD is observed for all event of inflow angle exceeding 45º. Detailed study is required in the future to make clear the mechanism that causes the around-sill pathway.

5 Summary

The present study examined the seasonal pathway of the TWC and its response to rugged topography in the eastern mouth of the Tsugaru Strait. Surface currents used in examining these pathways were measured by HFR during the period 2014–2020. HFR clear captured the seasonal migration of the pathway, with northward migration during summer (41.64ºN) and southward migration during winter (41.55ºN). In addition, the TWC was intensified in the summer and autumn seasons (~ 1.00 m s^{-1}) and weakened in the winter season (~ 0.50 m s^{-1}). This seasonal variability correlated with SLDs between Fukaura and Hakodate. However,
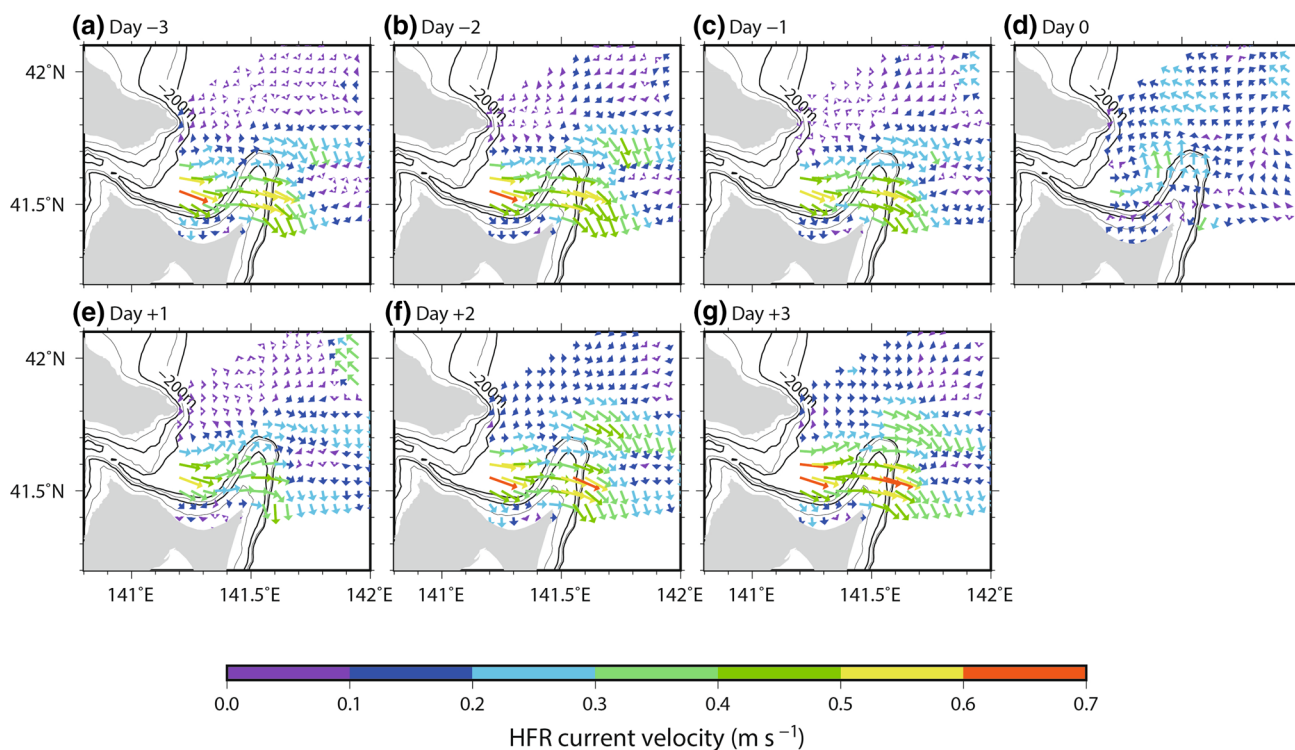
Fig. 16 Composite maps of daily-mean high-frequency ocean radar-based current velocity for periods during which inflow angle reached a local maximum exceeding 45º as calculated using data in Fig. 14. Data for 10 events (open square symbols in Fig. 14) are averaged here. Lapse time from day of peak inflow angle as **a** Day − 3, **b** Day − 2, **c** Day − 1, **d** Day 0, **e** Day 1, **f** Day 2, **g** Day 3 are considered

no statistically significant correlation was found at the eastern exit of the strait, where the seafloor extending from a sharp peninsula is shallower than in the surrounding region. Local flow amplification at a sill ridge was observed during autumn and winter, when the TWC assumed its Coastal mode, with flow confined near the coast. Such response of the TWC to the sill topography was not observed during summer, as the TWC moved away from the southern coast to pass through deep water. Even during Coastal mode, on some occasions the TWC did not pass over the sill instead took a pathway around the sill. This pattern was observed when the TWC was weak, a weak Coastal mode.

A locally strong barotropic current at shallow seafloor depths in the Tsugaru Strait may cause strong vertical mixing that contributes to the supply of near-bottom materials to the near-surface, as in the Bering Strait (Abe et al. 2019). Furthermore, an internal wave arrest point occurs in the lee of the sill; this breakup process may serve as an additional cause of vertical mixing.

Finally, our effort to evaluate/improve accuracy of HFR current data is underway. We chose four longitudinal lines from Line 1 to Line 4 to examine correlation with the SLD. However, our analysis showed that HFR data west of the Line 1 sometimes exhibited unrealistic value which encouraged us not to use data west of 141.2ºE. Uncertainty may be

included at Line 1 as well. This would have no large impact on changing our basic story, but these uncertainties should be made clear in the future for our science and safer and better ship navigation in this international strait.

References

Abe H, Sampei M, Hirawake T, Waga H, Nishino S, Ooki A (2019) Sediment-associated phytoplankton release from the seafloor in

response to wind-induced barotropic currents in the Bering Strait. Front Mar Sci 6:97. https://doi.org/10.3389/fmars.2019.00097

Abe H, Sasaki K, Yasui T, Wakita M (2020) Observation of Tsugaru warm current by high frequency radar and preliminary result for its prediction. Kaiyo Monthly 52(7):312–316 ((**in Japanese**))

Barrick DE, Lipa BJ (1997) Evolution of bearing determination of HF current mapping radars. Oceanography 10:72–75

Barrick DE, Evans MW, Weber BL (1977) Ocean surface currents mapped by radar. Science 198:138–144. https://doi.org/10.1126/science.198.4313.138

Conlon DM (1982) On the outflow modes of the Tsugaru Warm Current. Mer 20:60–64

Ebuchi N, Fukamachi Y, Ohshima KI, Shirasawa K, Ishikawa M, Takatsuka T, Daibo T, Wakatsuchi M (2006) Observation of the Soya Warm Current using HF ocean radar. J Oceanogr 62:47–61. https://doi.org/10.1007/s10872-006-0031-0

Fukudome K-I, Yoon J-H, Ostrovskii A, Takikawa T, Han I-S (2010) Seasonal volume transport variation in the Tsushima Warm Current through the Tsushima Straits from 10 years of ADCP observations. J Oceanogr 66:539–551. https://doi.org/10.1007/s10872-010-0045-5

Han S, Hirose N, Kida S (2018) The role of topographically induced form drag on the channel flows through the East/Japan Sea. J Geophys Res Oceans 123:6091–6105. https://doi.org/10.1029/2018JC013903

Hanawa K, Mitsudera H (1987) Variation of water system distribution in the Sanriku coastal area. J Oceanogr 42:435–446. https://doi.org/10.1007/BF02110194

Ida S, Yamashita S, Isoda Y, Kobayashi N (2016) Inflow process of low potential vorticity water originating from the intermediate waters of the Japan Sea into the Tsugaru Strait. Oceanogr Japan 25(4):101–122. https://doi.org/10.5928/kaiyou.25.4_101 (**in Japanese with English abstract**)

Iino R, Isoda Y, Yahaba H (2009) Sea level difference inducing the passage-flow through the Tsugaru Strait. Umi to Sora 85:1–19 ((**in Japanese with English abstract**))

Isobe A (1999) On the origin of the Tsushima Warm Current and its seasonality Cont. Shelf Res 19(1):117–133

Isoda Y, Baba K (1998) Tides and tidal currents in the Tsugaru Strait. Bull Facul Fish Hokkaido University 49(3):117–130 ((**in Japanese with English abstract**))

Ito T, Togawa O, Ohnishi M, Isoda Y, Nakayama T, Shima S, Kuroda H, Iwahashi M, Sato C (2003) Variation of velocity and volume transport of the Tsugaru Warm Current in the winter of 1999–2000. Geophys Res Lett 30:1678 (**HTTPS://doi.org/10.1029/2003GL017522**)

Kaneko H, Sasaki K, Abe H, Tanaka T, Wakita M, Watanabe S, et al (2021) The role of an intense jet in the Tsugaru Strait in the formation of the outflow gyre revealed using high-frequency radar data. Geophys Res Lett 48: e2021GL092909. https://doi.org/10.1029/2021GL092909

Kida S, Qiu B, Yang J, Lin X (2016) The annual cycle of the japan sea throughflow. J Phys Oceanogr 46:23–39. https://doi.org/10.1175/JPO-D-15-0075.1

Kobayashi N, Ohta S, Isoda Y, Shouji K, Kudou I, Aramaki T (2014) The bifurcation of the Tsugaru Gyre over the Hidaka shelf slope. Umi Sora (sea and Sky) 90:1–10

Kubokawa A (1991) On the behavior of outflows with low potential vorticity from a sea strait. Tellus 43A:168–176

Kuroda H, Isoda YM, Ohnishi M, Iwahashi M, Satoh C, Nakayama T, Ito T, Iseda K, Nishizawa K, Shima S, Togawa O (2004)

Examination of harmonic analysis methods using semi-regular sampling data from an ADCP installed on a regular ferry: Evaluation of tidal and residual currents in the eastern mouth of the Tsugaru Strait. Umi Kenkyu 13:553–564

Nishida Y, Kanomata I, Tanaka I, Sato S, Takahashi S, Matsubara H (2003) Seasonal and interannual variations of the volume transport through the Tsugaru Strait. Umi Kenkyu 12:487–499 ((**in Japanese with English abstract**))

Ohshima KI, Simizu D, Ebuchi N, Morishima S, Kashiwase H (2017) Volume, heat, and salt transports through the Soya Strait and their seasonable and interannual variations. J Phys Oceanogr 47:999–1019. https://doi.org/10.1175/JPO-D-16-0210.1

Ohta S, Isoda Y, Yoshimura S, Syouji K, Arita S, Kawano K, Xiaorong F, Kobayashi N (2015) Internal tidal waves generated over the sill topography in the Tsugaru Strait. Umi to Sora 90:63–68 (**in Japanese with English abstract**)

Ohtani K, Akiba Y, Yoshida K, Ohtsuki T (1971) Studies on the change of the hydrographic conditions in the Funka Bay III. Oceanic conditions of the Funka Bay occupied by the Oyashio waters. Bull Fac Fish Hokkaido Univ 22:129–142 ((**in Japanese with English abstract and legends**))

Paduan JD, Washburn L (2013) High-frequency radar observations of ocean surface currents. Annu Rev Mar Sci 5:115–136. https://doi.org/10.1146/annurev-marine-121211-172315

Pratt LJ, Lundberg PA (1991) Hydraulics of rotating strait and sill flow. Annu Rev Fluid Mech 23:81–106

Rosa AL, Isoda Y, Uehara K, Aiki T (2007) Seasonal variations of water system distribution and flow patterns in the southern sea area of Hokkaido, Japan. J Oceanogr 63:573–588. https://doi.org/10.1007/s10872-007-0051-4

Shimizu M, Isoda Y, Baba K (2001) A late winter hydrography in Hidaka bay, South of Hokkaido, Japan. J Oceanogr 57:385–395. https://doi.org/10.1023/A:1021585315008

Takikawa T, Yoon JH (2005) Volume transport through the Tsushima Straits estimated from sea level difference. J Oceanogr 61:699–708. https://doi.org/10.1007/s10872-005-0077-4

Takikawa T, Yoon J-H, Cho K-D (2005) The Tsushima warm current through Tsushima straits estimated from ferryboat ADCP data. J Phys Oceanogr 35:1154–1168. https://doi.org/10.1175/JPO2742.1

Thompson RO (1983) Low-pass filters to suppress inertial and tidal frequencies. J Phys Oceanogr 13:1077–1083. https://doi.org/10.1175/1520-0485(1983)013%3c1077:LPFTSI%3e2.0.CO;2

Toba Y, Tomizawa K, Kurasawa Y, Hanawa K (1982) Seasonal and year-to-year variability of the Tsushima–Tsugaru warm current system with its possible cause. Mer 20:41–51

Wakita M, Sasaki K, Nagano A, Abe H, Tanaka T, Nagano K, et al. (2021) Rapid reduction of pH and $CaCO_3$ saturation state in the Tsugaru Strait by the intensified Tsugaru Warm Current during 2012–2019. Geophys Res Lett 48: e2020GL091332. https://doi.org/10.1029/2020GL091332

Whitehead JA Jr, Miller AR (1979) Laboratory simulation of the gyre in the Alboran Sea. J Geophys Res 84(C7):3733–3742

Yoshikawa Y, Masuda A, Marubayashi K, Ishibashi M, Okuno A (2006) On the accuracy of HF radar measurement in the Tsushima Strait. J Geophys Res Oceans 111:C04009. https://doi.org/10.1029/2005JC003232

Zhang W, Ebuchi N, Fukamachi Y, Yoshikawa Y (2016) Estimation of wind drift current in the Soya Strait. J Oceanogr 72:299–311. https://doi.org/10.1007/s10872-015-0333-1